Band-edge positions in GW: Effects of starting point and self-consistency

Wei Chen and Alfredo Pasquarello

Chaire de Simulation à l'Echelle Atomique (CSEA), Ecole Polytechnique Fédérale de Lausanne (EPFL), CH-1015 Lausanne, Switzerland

(Received 4 July 2014; revised manuscript received 7 October 2014; published 27 October 2014)

We study the effect of starting point and self-consistency within GW on the band-edge positions of semiconductors and insulators. Compared to calculations based on a semilocal starting point, the use of a hybrid-functional starting point shows a larger quasiparticle correction for both band-edge states. When the self-consistent treatment is employed, the band-gap opening is found to result mostly from a shift of the valence-band edge. Within the non-self-consistent methods, we analyse the performance of empirical and nonempirical schemes in which the starting point is optimally tuned. We further assess the accuracy of the band-edge positions through the calculation of ionization potentials of surfaces. The ionization potentials for most systems are reasonably well described by one-shot calculations. However, in the case of TiO_2, we find that the use of self-consistency is critical to obtain a good agreement with experiment.

DOI: 10.1103/PhysRevB.90.165133 PACS number(s): 71.15.Dx, 31.15.E−, 71.10.−w

I. INTRODUCTION

Band-edge positions of solids, i.e., the valence-band maximum (VBM) and the conduction-band minimum (CBM), are fundamental to a variety of technologically relevant problems in condensed matter physics and material science. One of the most prominent examples is the band offset at the interface of a heterojunction [1–3]. The size of the band offset regulates the electrical properties of the heterojunction, and its determination depends to a large extent on the relative band-edge positions of the two components with respect to the electrostatic-potential lineup at the interface [2,4]. A similar scenario occurs at semiconductor-electrolyte interfaces, which are gaining attention for applications in solar energy conversion. Specifically, to achieve photocatalytic water splitting, the VBM and the CBM of the semiconducting photoelectrode need to straddle the hydrogen reduction and the water oxidation potentials [5]. Another class of applications involves the determination of defect energy levels in solids. For localized defects, the accuracy of the defect energy levels is closely associated to the band-edge positions predicted by the adopted theoretical scheme [6–10].

In spite of the ubiquity and elementary role of band edges in various applications, accurate determinations of their positions from theory remain difficult. For instance, band-edge positions through (semi)local density functional theory (DFT) are destined to be problematic as the band gap is severely underestimated. This is clearly manifested by the severely underestimated ionization potentials calculated within the Perdew-Burke-Ernzerhof (PBE) functional [11], implying that the alignment of the VBM with respect to the vacuum level is not correct at this level of theory [12]. More realistic band gaps can be achieved within the class of hybrid functionals, in which a fraction of Fock exchange is incorporated and admixed with (semi)local exchange [13]. The higher accuracy and particularly the ability to reproduce the experimental band gap have made the use of hybrid functionals a routine practice in electronic-structure calculations.

Many-body perturbation theory in Hedin's GW approximation is a formally more accurate approach to tackle the band-edge problem [14]. The exchange and correlation effects are taken into account by the electronic self-energy as the convolution of the Green's function G and the dynamically screened Coulomb interaction W. The obtained quasiparticle (QP) energies of the VBM and the CBM can be immediately interpreted as the ionization potential and electron affinity in photoemission experiments. While the GW approximation has shown great promise in the band-gap prediction for semiconductors and insulators, very few studies have been devoted to the band edges and the accuracy of GW band-edge positions remains unsettled [12,15]. In particular, as GW QP calculations are usually carried out perturbatively on top of the one-particle Kohn-Sham (KS) equation (denoted as G_0W_0 hereafter) [16], the QP spectrum of G_0W_0 is inevitably associated with the density functional starting point. The G_0W_0 starting from a semilocal functional description of the electronic structure has become the *de facto* standard for GW calculations nowadays. It yields reasonable band gaps for small-gap semiconductors, whereas for wide-gap insulators and semiconductors with shallow d electrons the achieved band gap is still sizably smaller than experiment [15,17], leading to ambiguity in the accuracy of the predicted band edges. Indeed, Jiang *et al.* showed that G_0W_0 on top of PBE is inclined to underestimate the ionization potentials of semiconductors as a consequence of the small size of the calculated band gaps [12].

To address the issue of the (semi)local starting point in G_0W_0, one could either use a starting point which gives an improved description of the electronic structure, or rely on a self-consistent scheme to get rid of the dependence on the starting point. In the former case, Fuchs *et al.* showed that G_0W_0 on top of hybrid functionals results in systematically more accurate band gaps and d-band binding energies compared to the semilocal starting point [18]. The latter approach, while being computationally much more demanding due to the self-consistent update of the energies and wave functions, provides an unbiased and accurate description of the band gap irrespective of the starting point [17,19–21].

In this paper, we investigate the effect of different starting points and the self-consistency within the GW approximation. We focus on the band-edge positions as obtained with the PBE0 hybrid functional [22], the perturbative G_0W_0 (either on top of PBE or of PBE0), and the quasiparticle self-consistent GW. We consider a series of representative materials, covering

simple *sp* semiconductors (Si, Ge, SiC, AlN, MoS_2, and C), semiconductors with shallow *d* electrons (GaAs, GaP, GaN, ZnO, and ZnSe), and wide-gap oxides and insulators (TiO_2, HfO_2, SiO_2, MgO, and LiF). In particular, we investigate the band-edge positions when the starting point of the G_0W_0 method is optimally tuned by varying the mixing parameter. Finally, the accuracy of the calculated band-edge positions is examined through ionization-potential calculations for surfaces.

This paper is organized as follows. In Sec. II, we outline the theoretical framework of the various schemes. In Sec. III, the detailed computational techniques and parameters are provided. We then discuss the band gaps in Sec. IV. The band-edge positions are studied in detail in Sec. V, and the performance of one-shot G_0W_0 schemes based on optimally chosen initial states is investigated in Sec. VI. The accuracy of band-edge positions is assessed in the context of ionization potentials in Sec. VII. Conclusions are drawn in Sec. VIII.

II. THEORETICAL FRAMEWORK

In this section, we briefly outline the different levels of theory used throughout this paper. We start with the KS density functional theory, the basis of all methods used in this paper. The KS eigenvalues ($\varepsilon_n^{\rm KS}$) are found by solving the equation (in atomic units)

$$\left\{-\tfrac{1}{2}\nabla^2 + v_{\rm ext}(\mathbf{r}) + v_{\rm H}(\mathbf{r}) + v_{\rm xc}(\mathbf{r}) - \varepsilon_n^{\rm KS}\right\}|\psi_n(\mathbf{r})\rangle = 0, \qquad (1)$$

where $v_{\rm ext}(\mathbf{r})$ and $v_{\rm H}(\mathbf{r})$ are the external potential and the Hartree potential, respectively. The exchange-correlation effect is accounted for in $v_{\rm xc}(\mathbf{r})$.

In the PBE0 hybrid functional, a fraction α (0.25 by default) of Fock exchange Σ_x is mixed with the PBE exchange $v_x^{\rm PBE}(\mathbf{r})$, giving rise to a nonlocal exchange v_x:

$$v_x(\mathbf{r},\mathbf{r}') = \alpha\Sigma_x(\mathbf{r},\mathbf{r}') + (1-\alpha)v_x^{\rm PBE}(\mathbf{r}). \qquad (2)$$

The shift $\Delta\varepsilon_n$ of the band-edge state $|n\rangle$ with respect to the PBE calculation is obtained as

$$\Delta\varepsilon_n = \left(\varepsilon_n^{\rm PBE0} - V_{\rm ref}^{\rm PBE0}\right) - \left(\varepsilon_n^{\rm PBE} - V_{\rm ref}^{\rm PBE}\right), \qquad (3)$$

where ε_n is the eigenvalue of the state $|n\rangle$, and $V_{\rm ref}$ refers to a universal reference level in both calculations. However, the universal reference level is ill defined in a three-dimensional periodic system as the potential energy is determined up to a constant. Here, we take for $V_{\rm ref}$ the averaged sum of the electrostatic potential and the local potential. As will be shown in Sec. VII for surfaces, $V_{\rm ref}$ defined with respect to the common vacuum level does not change by more than 0.1 eV when going from PBE to PBE0. As such, the difference in $V_{\rm ref}$ in Eq. (3) can be safely discarded, and the band-edge shift can be obtained as the eigenvalue difference provided the same alignment convention is adopted in the two bulk calculations. When performed perturbatively, Eq. (3) can then be expressed as

$$\Delta\varepsilon_n = \alpha\langle n|\Sigma_x(\mathbf{r},\mathbf{r}') - v_x^{\rm PBE}(\mathbf{r})|n\rangle, \qquad (4)$$

and the shift is hence proportional to α.

In the one-shot GW calculations, QP corrections to the band edges are obtained through the Taylor expansion of the self-energy $\Sigma(\mathbf{r},\mathbf{r}')$ around the (generalized) KS (e.g., PBE or PBE0) eigenvalue

$$\Delta\varepsilon_n = Z_n\langle n|\Sigma\left(\mathbf{r},\mathbf{r}';\varepsilon_n^{\rm KS}\right) - v_{\rm xc}(\mathbf{r})|n\rangle, \qquad (5)$$

where Z_n is the renormalization factor defined as $(1-\partial\Sigma/\partial E)^{-1}|_{E=\varepsilon_n^{\rm KS}}$. The self-energy is a product of the Green's function G and the screened Coulomb interaction $W=\varepsilon^{-1}v$, with v being the bare Coulomb interaction. The dielectric screening $\varepsilon^{-1}=1+v\chi$ is obtained using the random phase approximation (RPA) for the polarizability χ.

To go beyond the G_0W_0, we adopt the concept of the QP self-consistent GW approximation (QSGW) of Faleev, van Schilfgaarde, and Kotani [19,20,23]. The idea is to find an optimum noninteracting Hamiltonian within the QP picture using Hedin's GW approximation. For a set of trial QP eigenvalues and amplitudes $\{\varepsilon_i,|i\rangle\}$, one choice of such a model self-energy is proposed as

$$\langle i|\overline{\Sigma}|j\rangle = \tfrac{1}{2}{\rm Re}[\langle i|\Sigma(\varepsilon_i)|j\rangle + \langle j|\Sigma(\varepsilon_j)|i\rangle], \qquad (6)$$

where Re implies that the Hermitian parts of the matrix are taken. A new set of orthogonal QP amplitudes can be obtained by diagonalizing $\overline{\Sigma}$, which gives rise to a new electron density and corresponding Hartree potential, and eventually a new $\overline{\Sigma}$. This procedure is carried out iteratively until the QP energies are converged. We note that in this paper, both QP energies and wave functions are updated. On the other hand, the screened interaction W can be either updated self-consistently or fixed at the PBE level ($W_0^{\rm PBE}$) with no further iteration. Interestingly, the latter often leads to a more favorable agreement with experimental band gaps than using the self-consistent W in QSGW [17]. This is tentatively attributed to the lack of the electron-hole interaction (or vertex correction) in the polarizability χ within the RPA, which underestimates the dielectric screening and thereby overshoots the band gap in QSGW [17,20]. Indeed, to some extent, the static dielectric constant $\varepsilon_\infty(\omega=0)$ obtained through a semilocal functional (e.g., PBE) agrees well with that calculated from the self-consistent W with vertex corrections [17]. This justifies the practice of fixing W at $W_0^{\rm PBE}$ for band-gap predictions. In this paper, we provide both the full QSGW and the QS$GW_0^{\rm PBE}$ results.

We finally note that the QSGW is different from the fully self-consistent GW where the Dyson equation for the Green's function $G=G_0+G_0\Sigma G$ is directly updated in terms of the GW self-energy and the noninteracting Green's function G_0 [24]. Compared to the fully self-consistent GW, QSGW has been shown to produce more accurate band gaps and bandwidths [20]. For this reason, we here adopt the QSGW technique to investigate the effect of self-consistency in the GW approximation.

III. COMPUTATIONAL DETAILS

A. Pseudopotentials

Our calculations use the plane-wave basis set implementation in ABINIT [25]. Core-valence interactions are described by norm-conserving pseudopotentials (NCPPs). The reference

TABLE I. Setup of the norm-conserving pseudopotentials used in this paper. The angular momentum l of the local channel, cutoff radius r (in bohr), and the kinetic energy cutoff $E_{\rm cut}$ (in Ry) are given.

	Valence	l (local)	r_s	r_p	r_d	$E_{\rm cut}$
Si	$2s2p$	1	1.95	1.95		50
Ge	$3s3p4s4p3d$	1	0.80	0.80	0.80	330
Ga	$3s3p4s4p3d$	1	0.80	0.80	0.80	330
As	$4s4p$	0	1.58	1.75		100
Mo	$4s4p5s4d$	0	1.50	1.60	1.70	80
N	$2s2p$	0	1.35	1.54		65
P	$3s3p$	0	1.40	1.45		50
Al	$2s2p3s3p$	0	0.97	0.97		180
Ti	$3s3p4s4p3d$	0	1.28	1.28	1.70	100
Zn	$3s3p4s4p3d$	1	0.80	0.80	0.80	330
O	$2s2p$	2	1.15	1.25		80
Se	$4s4p$	1	1.82	1.95		100
C	$2s2p$	2	1.45	1.55		50
Hf	$5s5p6s5d$	0	1.78	1.80	1.80	65
Mg	$2s2p3s3p$	2	1.00	1.15		150
Li	$1s2s2p$	0	1.05	1.05		150

TABLE II. Crystal structures, lattice parameters a and c (in Å), and **k**-point samplings (Γ centered) used in the calculations. Additionally, the number of the bands ($n_{\rm b}$) used in the GW calculations is given.

	Structure	a	c	**k** points	$n_{\rm b}$
Si	Diamond	5.475		$8\times8\times8$	250
Ge	Diamond	5.658		$8\times8\times8$	750
GaAs	Zinc-blende	5.648		$8\times8\times8$	750
GaP	Zinc-blende	5.511		$8\times8\times8$	750
GaN	Wurtzite	3.215	5.237	$6\times6\times6$	750
AlN	Zinc-blende	4.412		$6\times6\times6$	600
TiO_2	Rutile	4.642	2.964	$5\times5\times7$	900
MoS_2	Hexagonal	3.216	12.541	$6\times6\times2$	900
ZnO	Wurtzite	3.279	5.288	$6\times6\times4$	900
ZnSe	Zinc-blende	5.716		$6\times6\times6$	800
SiC(4H-)	Hexagonal	3.096	10.138	$6\times6\times3$	500
C	Diamond	3.559		$6\times6\times6$	250
HfO_2	Fluorite	5.000		$6\times6\times6$	500
SiO_2	β-cristobalite	7.506		$4\times4\times4$	2000
MgO	Rocksalt	4.260		$6\times6\times6$	500
LiF	Rocksalt	4.069		$6\times6\times6$	500

configurations, the cutoff core radii, and the kinetic energy cutoffs of the NCPPs are listed in Table I. The quality of the NCPPs is of vital importance, in particular for GW calculations. Since the evaluation of both the polarizability and the self-energy requires the sum over a large number of unoccupied states, we construct the NCPPs so that their scattering properties are accurate up to 10 Ry above the vacuum level. This leads to small cutoff radii and high cutoff energies. In addition, for systems with Ga and Zn, it is necessary to include the $3s$ and the $3p$ shells among the valence states in order to give a reasonable $3d$ binding energy and band gap [26]. For the sake of consistency, a similar valence configuration is also applied to Ge, even though these semicore states have much less influence on the band edges since the localized $3d$ states of Ge lie much deeper [27]. For cationic species (Li, Mg, and Al), semicore states are also considered explicitly. The present setup of NCPPs ensures a highly faithful description of the electronic structures in both ground-state and excited-state calculations.

B. Ground-state calculations

We use the PBE exchange-correlation functional for the semilocal DFT calculations. Lattice parameters are determined from the PBE ground-state calculations for most materials, except for GaAs and Ge for which the experimental lattice constants are used, as their band gaps are very sensitive to the variation of the lattice constant. Using the PBE lattice constants for GaAs and Ge results in too small band gaps, even in the QSGW method. The crystal structures, lattice parameters, and **k**-point samplings used in the Brillouin zone (BZ) integration are listed in Table II.

Our hybrid-functional calculations use the PBE0 functional, which by default combines 25% of Fock exchange with 75% PBE exchange. The PBE correlation is retained in the PBE0. We note that the present implementation of PBE0 is conceptually akin to the QSGW. Instead of the full GW self-energy, only the exchange part $\Sigma_x = iGv$ of the self-energy enters the model self-energy in Eq. (6). It follows immediately that the new model self-energy is Hermitian by construction and corresponds exactly to the Fock exchange. Analogous to QSGW, the eigenvalues and wave functions are started from the PBE input and iterated until self-consistency is reached. Moreover, calculations with only the first iteration correspond to the one-shot or non-self-consistent PBE0 calculations [28,29]. To evaluate Fock exchange, we use the regular **q** points generated from the same **k**-point meshes as in the PBE calculations. The singularity appearing in the Fock exchange is treated by the auxiliary-function technique of Gygi and Baldereschi [30]. The **k**-point convergence issue will be discussed in detail in Sec. III D.

C. GW quasiparticle calculations

A central quantity in the GW approximation is the screened Coulomb interaction W, which is nonlocal and dynamic. Here, we adopt a full frequency treatment within the contour deformation technique to calculate the frequency dependence of the polarizability within the RPA [31]. This implies that the self-energy is also calculated with the explicit frequency dependence. Although a plasmon-pole model (e.g., that of Godby and Needs [32]) is often good for states in the vicinity of the Fermi level [33–35], it becomes inadequate in QSGW where the states far from the band edges also need to be considered. In general, we find that about 20 (10) frequency points along the real (imaginary) axis are sufficient for the QP energies to converge within 0.02 eV. We constantly use an energy cutoff of 30 Ry for the dielectric matrix. The dielectric matrices are evaluated on Γ-centered **k**-point meshes, except in the case of ZnO for which a shifted mesh is used to accelerate the convergence. For certain systems, in particular those with shallow $3d$ electrons, a very large cutoff energy of over 300 Ry is needed for the pseudopotentials. Nevertheless,

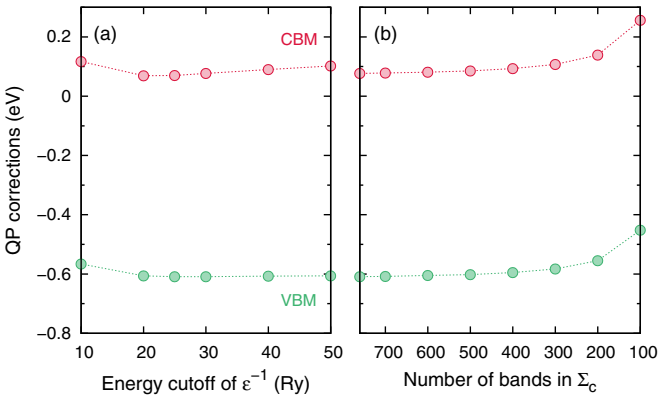

FIG. 1. (Color online) (a) Convergence of the G_0W_0 QP corrections to the VBM and CBM of GaAs with respect to the energy cutoff of the dielectric matrix ε^{-1}, and (b) convergence of the QP corrections with respect to the number of bands used in the self-energy. In (a), we use 750 bands in the self-energy. In (b), the energy cutoff of the dielectric matrix is taken at 30 Ry.

even for these materials, we find that an energy cutoff of 30 Ry for the dielectric function is sufficient for achieving well-converged band-edge energies. This is clearly seen in the case of GaAs shown in Fig. 1(a). For ZnO, a good convergence with a cutoff of 30 Ry in the dieletric function has also been demonstrated [34]. It should be pointed out that the relatively low cutoffs required for the dielectric function stem from the use of the contour deformation method [34]. The use of the Hybertsen-Louie plasmon-pole model is known to require higher cutoff values [34,36].

Another important parameter relates to the number of unoccupied states entering W and Σ. We include unoccupied states with energies up to 400 eV in our G_0W_0 calculations, equivalent to a total number of about 500 to 2000 bands (occupied and unoccupied) depending on the materials. In Fig. 1(b), we show the convergence of the QP energies of the VBM and the CBM with respect to the number of bands included in the GW self-energy for GaAs. Both band-edge energies are already well converged with 500 bands. For the highly demanding QSGW calculations, we only update and diagonalize the subspace of the lowest ∼100 to 150 bands and keep the higher-lying states at the PBE level. We estimate that the QP energies are converged within 0.05 eV within the current calculation scheme.

Table III summarizes the various GW approaches along with the nomenclature used in this paper. The one-shot method starts either from a PBE calculation, or a PBE0(α) calculation with the mixing parameter α. $G_0W_0(0)$ hence corresponds to the widely used G_0W_0 method on top of PBE, and $G_0W_0(0.25)$ stands for the one-shot G_0W_0 calculation on top of standard PBE0. In some cases, we purposely keep the PBE eigenvalues in the calculation of the polarizability for reasons already mentioned in Sec. II.

TABLE III. Nomenclature of various GW methods used in this paper. α denotes the fraction of Fock exchange used in the hybrid-functional (PBE0) starting point.

Notation	Type	Starting point
$G_0W_0(0)$	One-shot	PBE
$G_0W_0(\alpha)$	One-shot	PBE0(α)
$G_0W_0^{\mathrm{PBE}}(\alpha)$	One-shot	PBE0(α) for G; PBE for W
QSGW	Self-consistent	PBE
QSGW_0^{PBE}	Self-consistent	W fixed at the PBE level

D. Coulomb singularity and k-point convergence

As mentioned in Sec. III B, there is a singularity in the Fock exchange, for which the (diagonal) matrix element can be expressed in the form [31]

$$\langle \mathbf{k},n|\Sigma_x|\mathbf{k},n\rangle = -\frac{4\pi}{\Omega}\sum_{\mathbf{q}}\sum_{m}^{\mathrm{occ}}\sum_{\mathbf{G}}\frac{\left|M_{\mathbf{G}}^{mn}(\mathbf{k},\mathbf{q})\right|^2}{|\mathbf{q}+\mathbf{G}|^2}, \quad (7)$$

where the summation runs over all occupied states, Ω is the volume of the unit cell, and $M_{\mathbf{G}}^{mn}(\mathbf{k},\mathbf{q}) = \langle \mathbf{k}-\mathbf{q},n|e^{-i(\mathbf{q}+\mathbf{G})\mathbf{r}}|\mathbf{k},m\rangle$. The matrix element contains a singularity for $\mathbf{G}=\mathbf{0}$ and $m=n$, and diverges as $1/q^2$ for $\mathbf{q}\to 0$. The singularity leads to a slow convergence of the Fock exchange with respect to the number of $\mathbf{k}$ points, and it affects the determination of the VBM in the hybrid-functional calculation [37]. Gygi and Baldereschi showed that the divergence can be circumvented by introducing an auxiliary function $f(\mathbf{q})$ [30]. The auxiliary function should exhibit the same $1/q^2$ divergence as $\mathbf{q}\to 0$ but be smooth elsewhere. Adding and removing $f(\mathbf{q})$ eliminates the divergent term ($\mathbf{G}=\mathbf{0}$) in the summation [37,38]:

$$-\frac{4\pi}{\Omega}\sum_{m}\sum_{\mathbf{q}\neq 0}\left[\frac{\left|M_{\mathbf{0}}^{mm}\right|^2}{|\mathbf{q}|^2}-\left|M_{\mathbf{0}}^{mm}\right|^2 f(\mathbf{q})\right] -\frac{4\pi}{\Omega}\sum_{m}\left|M_{\mathbf{0}}^{mm}\right|^2\int_{\mathrm{BZ}} d\mathbf{q}\, f(\mathbf{q}). \quad (8)$$

Here, we demonstrate the treatment of the singularity using two different auxiliary functions. One general choice of the auxiliary function first adopted by Gygi and Baldereschi has the form [39,40]

$$f^{\mathrm{GB}}(\mathbf{q}) = \sum_{\mathbf{G}}\frac{e^{-\gamma|\mathbf{q}+\mathbf{G}|^2}}{|\mathbf{q}+\mathbf{G}|^2}, \quad (9)$$

where γ controls the width of the Gaussian and can be optimized to accelerate the convergence. For this auxiliary function, the mean value over the BZ reads as

$$\int_{\mathrm{BZ}} d\mathbf{q} f^{\mathrm{GB}}(\mathbf{q}) = 2\pi\sqrt{\pi/\gamma}. \quad (10)$$

The other auxiliary function that we use has been proposed by Carrier and Görling and reads as [38]

$$f^{\mathrm{CG}}(\mathbf{q}) = (2\pi)^2\left\{4\sum_{j=1}^{3}[\mathbf{b}_j\sin(\mathbf{a}_j\cdot\mathbf{q}/2)]^2 + 2\sum_{j=1}^{3}[\mathbf{b}_j\sin(\mathbf{a}_j\cdot\mathbf{q})]\cdot[\mathbf{b}_{j+1}\sin(\mathbf{a}_{j+1}\cdot\mathbf{q})]\right\}^{-1}, \quad (11)$$

where $\mathbf{a}_j(\mathbf{a}_1 \equiv \mathbf{a}_4)$ are the lattice vectors, and $\mathbf{b}_j$ are the corresponding reciprocal lattice vectors. The numerical integration of $f^{\mathrm{CG}}(\mathbf{q})$ over the BZ can be performed iteratively on an adaptive grid.

In GW calculations, apart from the bare exchange, the correlation part of the self-energy also possesses an integrable divergence. The matrix element of the correlation part Σ_c can be expressed as [40]

$$\langle \mathbf{k},n|\Sigma_c(\omega)|\mathbf{k},n\rangle = \frac{2i}{\Omega}\sum_{\mathbf{q}}\sum_{m}\sum_{\mathbf{G}_1\mathbf{G}_2}\frac{\left[M^{mn}_{\mathbf{G}_1}(\mathbf{k},\mathbf{q})\right]^* M^{mn}_{\mathbf{G}_2}(\mathbf{k},\mathbf{q})}{|\mathbf{q}+\mathbf{G}_1||\mathbf{q}+\mathbf{G}_2|} \times \int d\omega' \frac{\varepsilon^{-1}_{\mathbf{G}_1\mathbf{G}_2}(\mathbf{k}-\mathbf{q},\omega') - \delta_{\mathbf{G}_1\mathbf{G}_2}}{\omega+\omega'-\epsilon_{\mathbf{k}-\mathbf{q}m} \pm i\eta}, \quad (12)$$

where the sum runs over all the states, $\epsilon_{\mathbf{k}-\mathbf{q}m}$ is the energy of the state $|\mathbf{k}-\mathbf{q},m\rangle$, and η is positive infinitesimal. The $1/q^2$ divergence in the correlation self-energy for $\mathbf{G}_1,\mathbf{G}_2 = 0$ and $m = n$ can be treated with the same technique as described in Eq. (8) for the bare exchange.

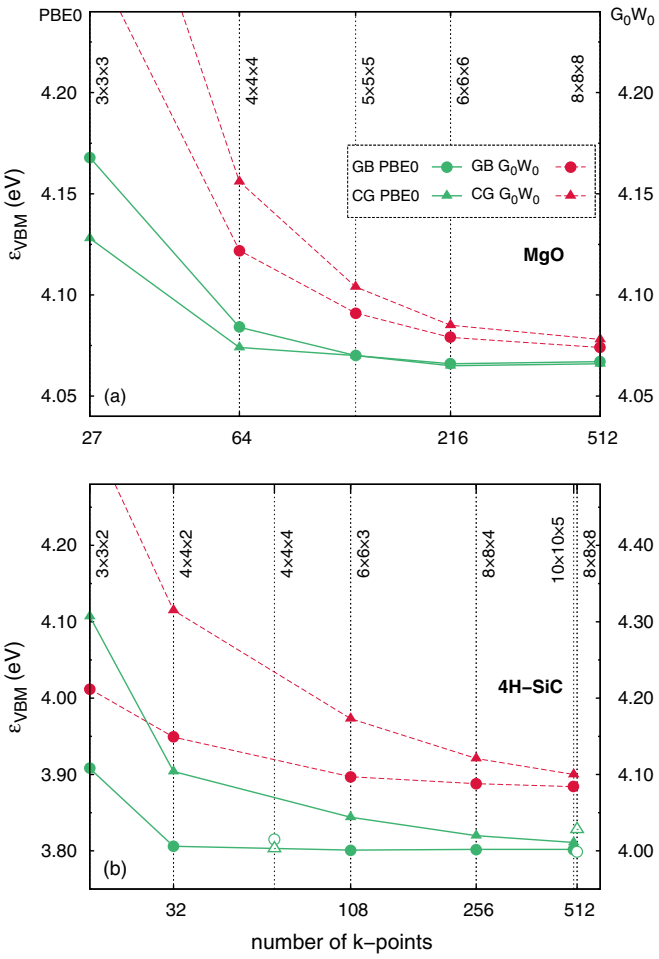

FIG. 2. (Color online) Convergence of the VBM energies with respect to the number of **k** points in the PBE0 and the G_0W_0 calculations. Triangles and disks correspond to the use of Carrier-Görling (CG) and Gygi-Baldereschi (GB) auxiliary functions. For 4H-SiC, the PBE0 values using the anisotropic meshes ($4\times4\times4$ and $8\times8\times8$) are denoted with open symbols. The eigenvalues are aligned through the local reference potential.

Figure 2 shows the **k**-point dependence of the VBM energies using the two auxiliary functions in the PBE0 and G_0W_0 calculations. Two typical materials, the semiconductor 4H-SiC and the oxide MgO, are used for illustration. The parameter γ is fixed to $150/E_{\mathrm{cut}}$, where E_{cut} is the exchange cutoff energy (in Hartree). For the MgO, both functions enable a rapid convergence of the VBM energies. The $6\times6\times6$ mesh is sufficient for a full convergence in the PBE0 and the G_0W_0 calculations. At variance, for the 4H-SiC, $f^{\mathrm{GB}}(\mathbf{q})$ shows a superior performance (full convergence with a $6\times6\times3$ mesh) and it works equally well with the anisotropic $(n\times n\times n)$ **k**-point meshes. The use of the $f^{\mathrm{CG}}(\mathbf{q})$ function does not guarantee the convergence within 0.01 eV in the G_0W_0 calculation, not even with a $10\times10\times5$ mesh. The convergence is also unsatisfactory with the anisotropic meshes. Throughout this paper, we adopt the Gygi-Baldereschi auxiliary function $f^{\mathrm{GB}}(\mathbf{q})$ to treat the singularity in PBE0 and G_0W_0 calculations.

IV. BULK BAND GAPS

We first assess the band gaps of the bulk systems. The KS and QP band gaps obtained from various methods are given in Table IV, and the comparison with experimental data is shown in Fig. 3. Band gaps predicted by the PBE functional are considerably smaller than experiment by a mean absolute relative error (MARE) of 46%. It should be borne in mind that the KS single-particle band gap does not correspond to the fundamental band gap probed in photoemission experiments [53–55]. Most of the error in the predicted band gap arises from the derivative discontinuity in the potential [56,57]. The residual errors are ascribed to the self-interaction error inherent to approximate density functionals [58]. Incorporating Fock exchange in the hybrid functional PBE0 significantly increases the band gap. With the default mixing parameter $\alpha = 0.25$, the PBE0 tends to overestimate the band gaps of semiconductors, but for wide-gap insulators the band gaps are still underestimated. In other words, the optimal α is material dependent [2,6,22]. The rationale of choosing the optimal α is related to the dielectric screening ε^{-1} of the material [2,59]. A smaller α is suitable for small-gap semiconductors, whereas wide-gap insulators need a much larger α to achieve the experimental band gaps.

We now turn to the GW band gaps. The one-shot G_0W_0 shows a considerable dependence on the starting point: G_0W_0 on top of PBE tends to underestimate the band gaps in particular for the wide-gap materials, while G_0W_0 on top of standard PBE0 results in an overall overestimation. For semiconductors, G_0W_0 typically leads to good agreement with experiment. Noticeable discrepancies are found for systems with the shallow d bands (e.g., GaN and ZnO). In particular, the band gap of ZnO has been a long-standing issue as the one-shot G_0W_0 on top of the semilocal functional underestimates the band gap by over 30%, unusually large for a semiconductor [34,60]. Its origin has been assigned to the spurious pd hybridization stemming from the underestimation of $3d$ binding energies [36]. The hybrid functional PBE0 lowers the localized $3d$ bands owing to the reduced self-interaction error, thereby serving as a better starting point for these materials. G_0W_0 rectifies the largely underestimated or

TABLE IV. Band gaps (in eV) calculated with PBE, PBE0(0.25), one-shot GW on top of PBE [$G_0W_0(0)$] or PBE0 [$G_0W_0(0.25)$], and self-consistent QSGW and QSGW_0^{PBE} methods. The absolute error (ME), mean absolute error (MAE), and the mean absolute relative error (MARE) are provided.

	PBE	PBE0(0.25)	$G_0W_0(0)$	$G_0W_0(0.25)$	QSGW_0^{PBE}	QSGW	Expt.
Si	0.67	1.84	1.26	1.75	1.37	1.54	1.17 [a]
Ge	0.00	1.32	0.63	1.00	0.77	0.90	0.74 [a]
SiC	2.25	3.87	3.08	3.74	3.31	3.80	3.30 [b]
AlN	3.33	5.26	4.81	5.79	5.07	5.37	4.90 [c]
C	4.22	6.17	5.62	6.34	5.86	6.43	5.48 [a]
GaAs	0.53	1.93	1.21	1.83	1.35	1.60	1.52 [a]
GaP	1.58	3.07	2.42	2.97	2.55	2.87	2.35 [d]
GaN	1.77	3.73	2.75	3.67	3.11	3.73	3.51 [c]
ZnO	0.78	3.01	2.02	3.32	2.81	4.36	3.44 [e]
ZnSe	1.23	2.92	2.28	3.06	2.56	3.26	2.80 [f]
MoS_2	0.87	1.96	1.39	1.69	1.29	1.40	1.29 [g]
TiO_2	1.86	4.02	3.27	3.96	3.37	4.23	3.30 [h]
HfO_2	4.08	6.38	5.67	6.63	6.38	7.38	5.8 [i]
SiO_2	5.33	7.77	8.36	9.39	8.76	10.50	8.90 [j]
MgO	4.38	6.80	6.71	8.02	7.29	9.07	7.80 [k]
LiF	8.85	11.85	13.13	14.43	14.29	16.17	14.20 [l]
ME (eV)	−1.80	0.09	−0.37	0.44	−0.02	0.76	
MAE (eV)	1.80	0.70	0.42	0.46	0.24	0.76	
MARE (%)	46.1	23.7	11.0	16.9	6.9	17.7	

[a]Reference [41].
[b]Reference [42].
[c]Reference [43].
[d]Reference [44].
[e]Reference [45].
[f]Reference [46].
[g]Reference [47].
[h]Reference [48].
[i]Reference [49].
[j]Reference [50].
[k]Reference [51].
[l]Reference [52].

overestimated band gaps obtained from PBE and PBE0 starting points, and provides a closer agreement with experiment.

The QSGW method systematically predicts larger band gaps with a MARE of 17% compared to experiment. This is a known behavior of the QSGW as the dielectric constants are typically overestimated, and it prompts some empirical practices of scaling the QP correction by a factor of 0.8 as in the hybrid QSGW scheme [61,62]. In fact, the achieved overestimation has been rationalized by effects that are beyond the treatment of the QSGW, including vertex corrections [63], lattice polarizations [64], and electron-phonon interactions [65,66]. To illustrate this point, we take diamond as an example, for which QSGW predicts a band gap of 6.4 eV. Shishkin *et al.* found that the vertex correction in the W reduces the gap by 0.4 eV [63]. Giustino *et al.* showed an anomalously large renormalization of 0.6 eV due to the electron-phonon coupling [65]. The lattice polarization does not contribute since diamond is nonpolar. As a whole, these effects lead to a 1.0-eV reduction in the QSGW band gap, bringing the theoretical band gap in excellent agreement with the experimental value (5.5 eV). As pointed out earlier [64], this shows that the overestimation is not due to the deficiency in the treatment of the electronic self-energy in the QSGW method, but rather to the lack of higher-order diagrammatic terms and to interactions with phonons. It is not trivial to take into account all these effects, but it has been argued that they can be accounted for by an effective dielectric screening, which can be achieved by the PBE description within the RPA [63]. Indeed, when the W is fixed at the PBE-RPA level (QSGW_0^{PBE}), the band gaps are systematically in much better agreement with experiment as evidenced by the MARE of 7%. However, the band gap of ZnO still remains unsatisfactory. The sizable discrepancies can be traced to the unrealistic dielectric constant which is either too low in QSGW ($\varepsilon_\infty = 2.1$) or too high in QSGW_0^{PBE} ($\varepsilon_\infty = 5.3$) compared to the experimental value of 3.7 [63]. Therefore, an explicit treatment of the vertex corrections and the phonon contribution turns out to be ineluctable for ZnO.

V. BAND-EDGE POSITIONS

Band-edge positions from the semilocal PBE calculations are deemed to be inaccurate due to the systematic underestimation of the band gaps as shown in Sec. IV. Here, we investigate the band-edge positions, or more specifically the band-edge shifts with respect to the PBE description through PBE0 and GW calculations with different levels of approximations. In

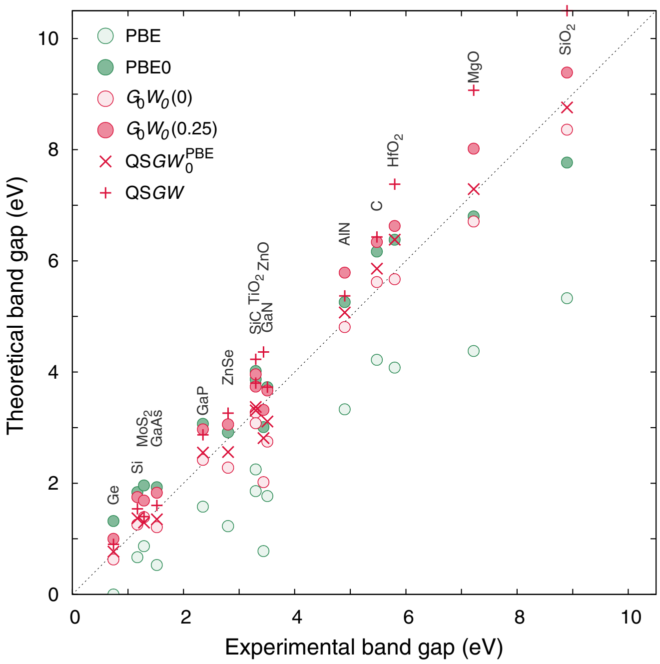

FIG. 3. (Color online) Band gaps (theoretical vs experimental) of various semiconductors and insulators. LiF is not included in here. The band-gap values are collected in Table IV.

addition to the absolute shifts of the VBM and the CBM, we introduce the relative band-edge shift with respect to the band-gap variation (e.g., $\delta_{\rm VBM}$ for the VBM) [7,15]. The materials considered here can be grouped into four categories in order of increasing band gaps: simple *sp* semiconductors, semiconductors with shallow $3d$ electrons, transition metal compounds, and *sp* oxides and insulators. In the following, we illustrate the band-edge shifts for each of these categories. The values of the band-edge shifts are summarized in Table V and shown graphically in Fig. 4. We note that this section aims at identifying the differences in the band-edge positions as they result from the application of various levels of theory. The accuracy of the predicted band-edge positions is then assessed in Sec. VII by direct comparison with experimental ionization potentials.

A. *sp* semiconductors

Simple *sp* semiconductors include Si, Ge, AlN, SiC, and diamond. In these materials, the VBM and CBM are characterized by the bonding and antibonding states of *p* orbitals, respectively. As shown in Fig. 4 and Table V, PBE0 opens the band gaps of these materials in a symmetric fashion, with the $\Delta\varepsilon_{\rm VBM}$ accounting for 50%–60% of the band-gap increase. The relative VBM shift enhances as the bonding has a stronger ionic character (as in AlN). These characteristic shifts are seen as the effect of the incorporated Fock exchange [cf. Eq. (3)].

The one-shot G_0W_0 shows a very different scenario as the VBM shift accounts for most of the band-gap opening irrespective of the starting point. The dominant VBM shift is most notable for small band-gap semiconductors (e.g., Si and Ge) where the QP correction to the CBM is appreciably smaller. The band-edge shift is somewhat less biased for diamond.

TABLE V. Band-edge shifts (in eV) with respect to PBE energy levels obtained with PBE0(0.25), one-shot GW on top of PBE [$G_0W_0(0)$] or PBE0 [$G_0W_0(0.25)$], and self-consistent QSGW and QS$GW_0^{\rm PBE}$. The relative shift of the VBM $\delta_{\rm VBM}$ (in %) is defined as $\Delta\varepsilon_{\rm VBM}/\Delta E_g$ where ΔE_g is the change in the band gap.

	PBE0(0.25)			$G_0W_0(0)$			$G_0W_0(0.25)$			QS$GW_0^{\rm PBE}$			QSGW		
	$\Delta\varepsilon_{\rm VBM}$	$\Delta\varepsilon_{\rm CBM}$	$\delta_{\rm VBM}$	$\Delta\varepsilon_{\rm VBM}$	$\Delta\varepsilon_{\rm CBM}$	$\delta_{\rm VBM}$	$\Delta\varepsilon_{\rm VBM}$	$\Delta\varepsilon_{\rm CBM}$	$\delta_{\rm VBM}$	$\Delta\varepsilon_{\rm VBM}$	$\Delta\varepsilon_{\rm CBM}$	$\delta_{\rm VBM}$	$\Delta\varepsilon_{\rm VBM}$	$\Delta\varepsilon_{\rm CBM}$	$\delta_{\rm VBM}$
Simple *sp* semiconductors															
Si	−0.68	0.53	−56	−0.66	−0.07	−112	−0.88	0.19	−82	−0.83	−0.13	−119	−0.91	−0.04	−105
Ge	−0.62	0.56	−53	−0.62	−0.14	−129	−0.95	−0.09	−110	−0.87	−0.24	−138	−0.93	−0.17	−122
SiC	−0.97	0.65	−60	−0.67	0.16	−81	−1.03	0.46	−69	−0.91	0.15	−86	−1.18	0.37	−76
AlN	−1.29	0.63	−67	−1.20	0.28	−81	−1.79	0.67	−73	−1.43	0.30	−83	−1.48	0.56	−73
C	−1.03	0.93	−53	−0.95	0.43	−69	−1.30	0.79	−62	−1.11	0.52	−68	−1.40	0.79	−64
$3d$ semiconductors															
GaAs	−0.71	0.70	−50	−0.61	0.07	−90	−0.89	0.41	−68	−0.77	0.05	−94	−0.92	0.15	−86
GaP	−0.78	0.53	−60	−0.77	−0.12	−118	−1.05	0.15	−88	−1.00	−0.22	−128	−1.14	−0.03	−103
GaN	−1.20	0.76	−61	−0.87	0.10	−90	−1.40	0.49	−74	−1.31	0.03	−98	−1.61	0.35	−82
ZnO	−1.61	0.63	−72	−1.08	0.17	−86	−1.81	0.73	−71	−1.88	0.15	−93	−2.75	0.83	−77
ZnSe	−1.02	0.71	−59	−0.93	0.12	−89	−1.28	0.55	−70	−1.18	0.14	−89	−1.53	0.49	−76
Transition-metal compounds															
MoS_2	−0.73	0.36	−67	−0.22	0.31	−42	−0.57	0.25	−70	−0.53	0.11	−83	−0.63	−0.10	−119
TiO_2	−1.26	0.90	−58	−0.40	1.01	−28	−0.95	1.16	−45	−0.94	0.57	−62	−1.37	1.00	−58
HfO_2	−1.39	0.91	−60	−0.94	0.66	−60	−1.50	1.05	−59	−1.69	0.62	−73	−2.12	1.18	−64
sp oxides and insulators															
SiO_2	−1.68	0.74	−69	−2.07	0.96	−68	−2.80	1.26	−69	−2.51	0.91	−73	−3.69	1.48	−71
MgO	−1.59	0.83	−66	−1.61	0.72	−70	−2.41	1.23	−66	−2.08	0.83	−72	−3.23	1.45	−69
LiF	−2.11	0.89	−72	−2.80	1.48	−65	−3.63	1.95	−65	−3.87	1.57	−71	−4.96	2.36	−68

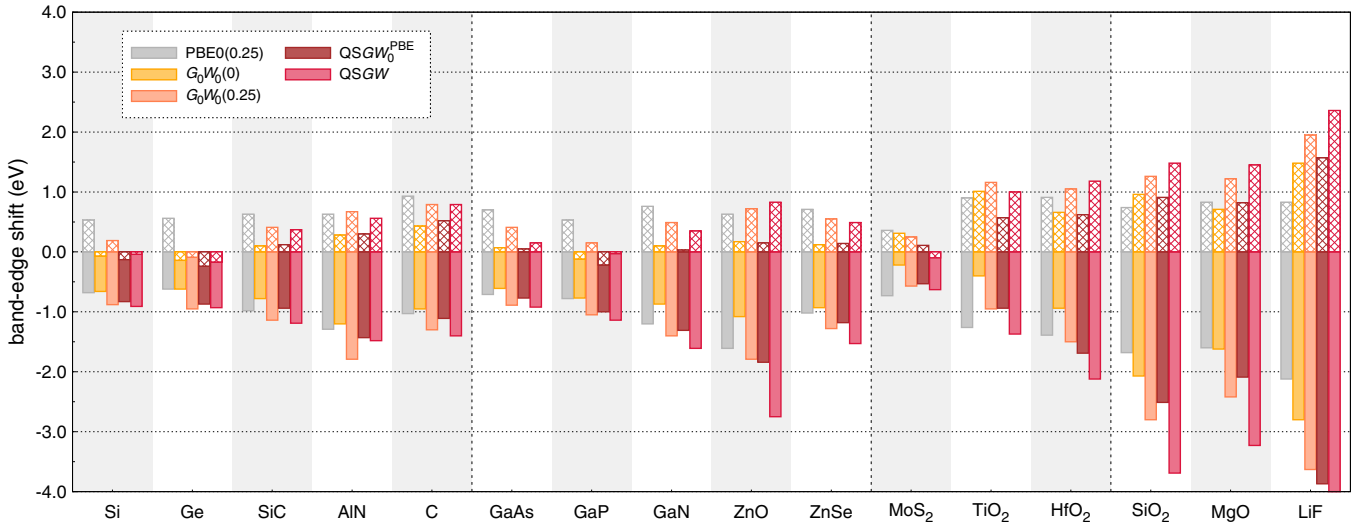

FIG. 4. (Color online) The VBM (solid-filled) and CBM (pattern-filled) shifts of the bulk materials relative to PBE references.

Including the self-consistency in QSGW_0^{PBE} and QSGW shows a more pronounced effect on the VBM than on the CBM. Compared to $G_0W_0(0)$, QSGW and QSGW_0^{PBE} give rise to a larger QP correction of VBM by ~ -0.2 to -0.4 eV, whereas the CBM is marginally shifted by typically less than 0.1 eV. On the whole, we see that all GW variants predict a predominant shift in the VBM for sp semiconductors, qualitatively at variance with the symmetric band-gap opening obtained with the hybrid functional.

B. 3*d* semiconductors

The 3d semiconductors (Ga- and Zn-based compounds) are characterized by the occurrence of shallow 3d electrons which hybridize with the p electrons of the anions. The VBM is, however, still mostly composed of p states, and the CBM has a mixed sp character. PBE0 yields a δ_{VBM} of -50% for GaAs and the value progressively reaches -71% for ZnO as the ionicity increases (cf. Table V).

In the one-shot $G_0W_0(0)$, the relative VBM shift turns out to be predominant, analogous to the sp semiconductors. The VBM-shift dominance is clearly visible in Fig. 4 regardless of the starting point, although the effect on δ_{VBM} is less pronounced in the $G_0W_0(0.25)$.

It is recognized that self-consistency is essential for these 3d semiconductors owing to the too shallow 3d bands in the semilocal description [17]. The band edges, in particular those of the valence band, are influenced by the 3d shell through the pd hybridization. The lowering of the VBM is accompanied by the shift of the 3d bands to deeper levels. In the case of ZnO, the self-consistency in QSGW_0^{PBE} leads to a further shift of the VBM by -0.4 eV relative to the one-shot $G_0W_0(0)$. The CBM is, however, less sensitive to the self-consistency. Meanwhile, we note that the self-consistency is also necessary in the PBE0 calculations of the 3d semiconductors. Compared to the perturbative PBE0, the self-consistent PBE0 shifts the VBM downward by 0.4 eV. These results substantiate that the prescription of self-consistency is essential in predicting the VBM position for 3d semiconductors. In terms of the relative band-edge shift, QSGW and QSGW_0 still favor the dominant role of the VBM, in line with the one-shot methods.

We remark that our current NCPP-based GW calculations disagree with a previous study adopting the projector-augmented-wave (PAW) formalism [15]. The discrepancy is particularly significant for 3d semiconductors. For instance, the PAW G_0W_0 finds a dominant QP correction to the CBM, distinctly different from the present NCPP result. Such a deviation is tentatively ascribed to the incomplete onsite basis sets of the partial waves, which affects the description of localized 3d states. The NCPP scheme does not suffer from such an incompleteness and therefore conceivably yields a more reliable QP correction to the band edges. The accuracy of the predicted band-edge shifts for GaAs will be further explored in the ionization potential calculation in Sec. VII.

C. Transition-metal compounds

A typical feature of transition-metal compounds (e.g., MoS_2, TiO_2, and HfO_2) that distinguishes themselves from other materials is the substantial d character in the CBM. The VBM consists of mainly p states of the anions. With PBE0, we see the usual pattern of the VBM shift relative to the band gap, ranging from about 60% to 70% of the band-gap variations. The situation is more diverse within the GW methods. We first discuss the case of rutile TiO_2. The one-shot $G_0W_0(0)$ on top of the PBE starting point assigns the majority of the band-gap opening to the QP correction in the CBM. The band-gap opening becomes more symmetric when one switches to the PBE0 starting point as in $G_0W_0(0.25)$ (cf. Fig. 4 and Table V). In addition, compared to the one-shot $G_0W_0(0)$, the incorporation of self-consistency in the QSGW_0^{PBE} significantly shifts the CBM of rutile downwards by 0.5 eV (cf. Fig. 4). As a result, the whole band structure of TiO_2 in QSGW_0^{PBE} is found to be about 0.5 eV lower than that in $G_0W_0(0)$. Such a pronounced downward shift of the CBM due to self-consistency is also present in the PBE0 calculation: the non-self-consistent PBE0 is found to place the CBM at an 0.8-eV higher energy with respect to the self-consistent one. This is likely associated with the inherent

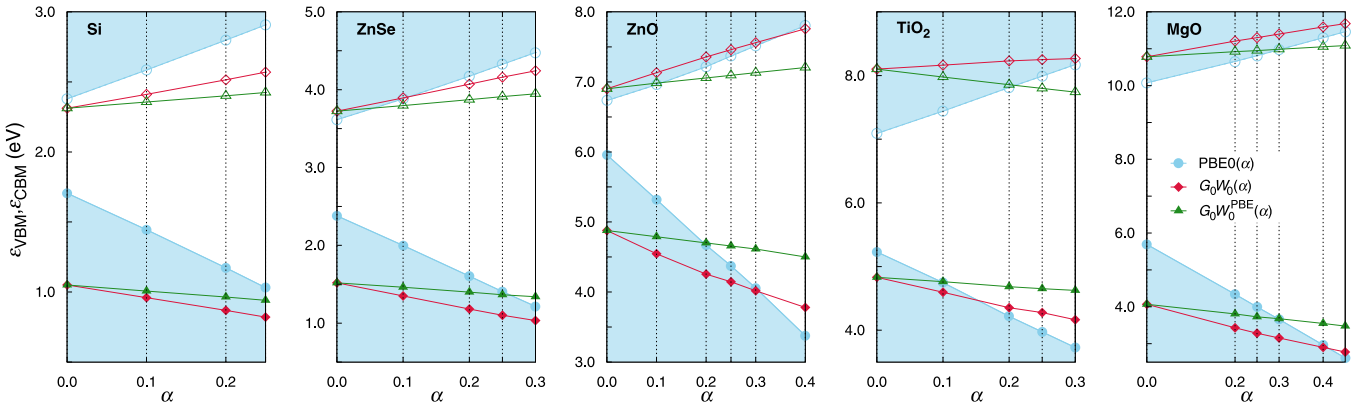

FIG. 5. (Color online) The VBM (filled symbols) and the CBM (open symbols) positions obtained by varying α in the PBE0 and the one-shot G_0W_0 calculations starting from the PBE0(α). In $G_0W_0^{\mathrm{PBE}}$, the screened interaction is fixed at the PBE level.

self-interaction error of semilocal functionals, affecting most notably the highly localized electronic states (e.g., Ti $3d$ states). We note that a similar decrease in the CBM energy of TiO_2 has been reported by Patrick and Giustino when Hubbard U corrections are included in the PBE starting point [67]. In addition, Marom *et al.* found that the PBE0 starting point gives a better agreement with experimental photoemission spectra for TiO_2 clusters [68]. It is thus persuasive to conclude that a starting point beyond the semilocal treatment is essential to describe the electronic structure of rutile TiO_2.

The scenario of TiO_2 discussed above is transferable to MoS_2. Notably, the QSGW_0^{PBE} band gap is even smaller than the $G_0W_0(0)$ one as a consequence of the drastic decrease of the CBM energy when self-consistency is initiated. In the case of HfO_2, self-consistency beyond PBE, however, has a much smaller effect on the CBM energy. Unlike TiO_2 and MoS_2 where the CBM is nearly of pure d character, the CBM of HfO_2 comprises a significant amount of O $2p$ states. For HfO_2, the PBE starting point is thus still adequate.

D. *sp* oxides and insulators

The remaining materials (e.g., SiO_2, MgO, and LiF) are highly ionic insulators. The VBM has a strong p character, and the CBM is characterized by hybridized sp orbitals. Interestingly, we observe a nearly constant δ_{VBM} of about -70% for these materials, irrespective of the adopted method and starting point. The PBE starting point therefore gives a satisfactory result for sp-bonded materials.

VI. DEPENDENCE ON THE MIXING PARAMETER α

The fraction of Fock exchange α in the PBE0 functional has been hitherto fixed at the default value (0.25). Varying the α modifies the eigenvalues of the starting point, thereby influencing the screening and the QP corrections of the ensuing G_0W_0 calculations. The effect of α on the ionization potentials of molecules and clusters has been demonstrated in the framework of G_0W_0 [69–71]. For solids, it is, however, unclear how the band-edge positions within the one-shot G_0W_0 are affected by the mixing parameter α in the starting point. To shed light on the dependence on α, we here choose five representative materials (Si, ZnSe, ZnO, TiO_2, and MgO) and show the α dependence of the band-edge positions within the hybrid-functional and the one-shot G_0W_0 schemes.

The evolution of the band-edge positions with respect to α is illustrated in Fig. 5. For the PBE0 calculations, the energies of VBM and CBM scale linearly with the mixing parameter α as is expected [6]. Within the one-shot G_0W_0 on top of PBE0, we also record a nearly linear evolution of the band-edge positions with respect to α. The dependence on α within the G_0W_0 scheme is, however, not as pronounced as that within PBE0. We further show the $G_0W_0^{\mathrm{PBE}}(\alpha)$ scheme in Fig. 5. A similar linear scaling of the band-edge energies is maintained within this scheme, while the band-edge positions become even less sensitive to α as a result of the stronger screening.

The observed dependence of the G_0W_0 band-edge positions raises a question: What is the best α for the starting point used in a one-shot G_0W_0 calculation? To shed light on this aspect, we next explore the possibilities of determining the optimal value of α based on two methodologies: an empirical and a nonempirical one. We are particularly interested in the band-edge positions given by the various choices of the optimal starting point.

A. Empirical tuning

In hybrid-functional calculations, the fraction of Fock exchange is often adjusted to reproduce the experimental band gap. Such a pragmatic approach is adopted when a realistic

TABLE VI. Valence band-edge shifts achieved with PBE0(α) and $G_0W_0(\alpha)$. The fraction of Fock exchange α is empirically tuned so that the calculated band gap E_g matches the experimental one.

	Empirical ($E_g \equiv E_g^{\mathrm{expt.}}$)				
	α^{PBE0}	$\alpha^{G_0W_0}$	$E_g^{\mathrm{expt.}}$	$\Delta\varepsilon_{\mathrm{VBM}}^{\mathrm{PBE0}}$	$\Delta\varepsilon_{\mathrm{VBM}}^{G_0W_0}$
Si	0.11	0.00	1.2	–0.3	–0.7
ZnSe	0.23	0.17	2.8	–0.9	–1.2
ZnO	0.30	0.27	3.4	–1.9	–1.9
TiO_2	0.17	0.01	3.3	–0.8	–0.4
MgO	0.35	0.21	7.8	–2.3	–2.3

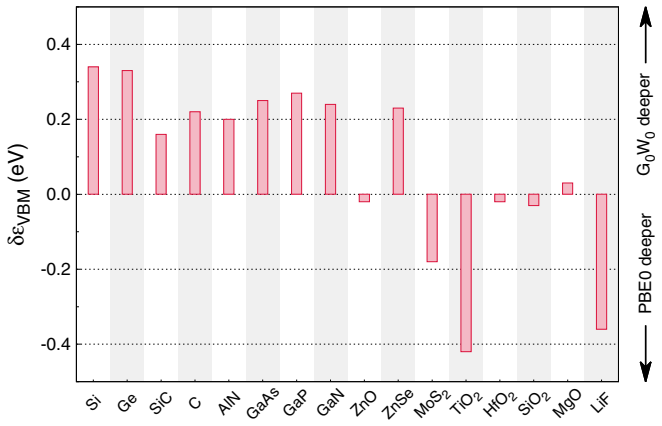

FIG. 6. (Color online) Discrepancies in the VBM positions between PBE0 and G_0W_0 calculations when both are empirically tuned to reproduce the experimental band gap. The eigenvalues are aligned through the local reference level. A positive (negative) value indicates that G_0W_0 predicts a deeper (higher) VBM compared to PBE0.

description of the band gap is appreciated. Following this strategy, the optimal mixing parameter α to be used in the PBE0(α) starting point for G_0W_0 can also be determined. As shown in Table VI, we obtain a vanishing α for Si since the PBE starting point already enables a good band gap. This is also true for rutile TiO_2, but the band-edge energies are shifted to higher values compared to the QS$GW_0^{\rm PBE}$ ones, as pointed out in Sec. V C. For ZnSe, ZnO, and MgO, an α between 0.2 to 0.3 satisfies the tuning criterion. We see that G_0W_0 requires a smaller amount of Fock exchange so as to reproduce the experimental band gap. The optimal α for a G_0W_0 calculation is typically below 0.3.

While empirically tuned PBE0 and G_0W_0 are designed to give the same band gap as experiment, there is no guarantee that the individual band-edge positions will also agree. To trace how the PBE0 band-edge positions deviate from the G_0W_0 ones, we plot the difference between the empirically tuned PBE0 and G_0W_0 calculations in Fig. 6. As shown in Fig. 6, for simple sp semiconductors, PBE0 is prone to place the VBM (or CBM) about 0.2 to 0.3 eV higher in energy compared to the tuned G_0W_0, consistent with the trend described in Sec. V A. Similar discrepancies have also been noticed for some other semiconductors [4]. At variance, the band-edge positions are deeper in PBE0 for the two transition-metal compounds, i.e., MoS_2 and TiO_2. Note that for these materials, the empirical G_0W_0 actually corresponds to the standard $G_0W_0(0)$ on top of the PBE electronic structure, which tends to overestimate the CBM energy (cf. Sec. V C). It is hence more relevant to use the QS$GW_0^{\rm PBE}$ as the GW reference for these two materials. In the case of rutile TiO_2, we indeed find a good alignment of band-edge positions between the empirical PBE0 and QS$GW_0^{\rm PBE}$ calculations, and the deviation of the associated VBM positions is less than 0.1 eV (cf. Table VI). Finally, we find that the empirically tuned PBE0 and G_0W_0 agree well in terms of band-edge positions for wide band-gap materials, except for LiF for which a deviation of ~0.4 eV is found.

B. Nonempirical tuning

We note that the practice of tuning α empirically is subject to ambiguities regarding the choice of the experimental reference. While the target quantity usually refers to the fundamental band gap, the true electronic band gap could differ due to the effects that are not included in our present study, such as electron-phonon interactions and lattice polarizations. These effects can lead to prominent band-gap renormalizations for wide-gap semiconductors and insulators [64,65]. Here, we consider two criteria for tuning the mixing parameter nonempirically within G_0W_0. First, we propose to define an optimal $\overline{\alpha}_A$ in the sense that it gives rise to the same band gap in the PBE0($\overline{\alpha}_A$) and the succeeding $G_0W_0(\overline{\alpha}_A)$ calculations. In other words, we look for an optimal starting point for the one-shot G_0W_0 calculation as far as the band gap is concerned. As shown in Table VII, $\overline{\alpha}_A$ ranges from 0.22 (for Si) to 0.45 (for MgO), and it is much higher than the α empirically tuned for G_0W_0. The ensuing band gaps are thereby systematically larger than the experimental values. Interestingly, we find that for most of the materials considered in this paper the band gaps obtained with the optimal $\overline{\alpha}_A$ agree with the QSGW ones within 0.2 eV (except for ZnO and TiO_2). Turning to the band-edge positions, we find a good agreement (within 0.2 eV on average) between the nonempirically tuned PBE0 and G_0W_0 calculations evaluated at $\overline{\alpha}_A$. The agreement is also preserved between the VBM positions calculated with $G_0W_0(\overline{\alpha}_A)$ and QSGW for materials other than ZnO and TiO_2 (cf. Table VII).

Alternatively, for the optimal mixing parameter to be used in the one-shot G_0W_0, one could rely on the band gap given by the QSGW calculation since the latter is completely parameter free. We designate this optimal mixing parameter by $\overline{\alpha}_B$. As shown in Table VII, the band-edge positions obtained from the tuned $G_0W_0(\overline{\alpha}_B)$ are commensurate to those from the QSGW, and the differences are typically no more than 0.2 eV. Hence, the nonempirically tuned hybrid-functional starting point enables the one-shot G_0W_0 to provide equivalent band-edge positions to those obtained with the much more demanding QSGW method.

One drawback of using the nonempirical tuning parameter $\overline{\alpha}_B$ is that the band gap is too large compared to experiment. We further propose a nonempirical tuning scheme which is based on the same tuning criterion as for $\overline{\alpha}_B$ but with the screened interaction kept at the PBE level, as the band gaps obtained with the QS$GW_0^{\rm PBE}$ method generally are in good agreement with experiment (cf. Sec. IV). The resultant optimal mixing parameter is denoted by $\overline{\alpha}_C$ in Table VII. In analogy with the previous nonempirical schemes, the deviations remain small between the VBM positions obtained with the tuned one-shot $G_0W_0(\overline{\alpha}_C)$ and the respective self-consistent scheme. For sp systems, the difference is typically less than 0.1 eV. Larger discrepancies are found for ZnO (0.4 eV) and TiO_2 (0.3 eV).

As a side note, we remark that the optimal mixing parameter α proposed in this section relies solely on the band gap as tuning criterion. The choice of such an optimal α is favorable in the context of band-edge positions, but it is less clear whether these optimal α also give rise to a reasonable description of other physical properties. To this end, we show in Table VIII the equilibrium lattice parameter a of the five representative

TABLE VII. Valence band-edge shifts achieved with PBE0($\overline{\alpha}$) and $G_0W_0(\overline{\alpha})$ when the fraction of Fock exchange $\overline{\alpha}$ is optimized through a nonempirical scheme. In scheme A, $\overline{\alpha}$ is optimized by ensuring that the same band gap E_g is achieved in PBE0($\overline{\alpha}$) and $G_0W_0(\overline{\alpha})$. In scheme B (C), $\overline{\alpha}$ is fixed by the condition that $G_0W_0(\overline{\alpha})$ achieves the same band gap as QSGW (QS$GW_0^{\rm PBE}$).

	Nonempirical A $E_g^{\rm PBE0} \equiv E_g^{G_0W_0}$				Nonempirical B $E_g^{G_0W_0} \equiv E_g^{\rm QS}GW$				Nonempirical C Same as B, but with $W_0^{\rm PBE}$			
	$\overline{\alpha}_A$	E_g	$\Delta\varepsilon_{\rm VBM}^{\rm PBE0}$	$\Delta\varepsilon_{\rm VBM}^{G_0W_0}$	$\overline{\alpha}_B$	E_g	$\Delta\varepsilon_{\rm VBM}^{G_0W_0}$	$\Delta\varepsilon_{\rm VBM}^{\rm QS}GW$	$\overline{\alpha}_C$	E_g	$\Delta\varepsilon_{\rm VBM}^{G_0W_0}$	$\Delta\varepsilon_{\rm VBM}^{\rm QS}GW_0$
Si	0.22	1.7	−0.6	−0.8	0.14	1.5	−0.8	−0.9	0.10	1.4	−0.7	−0.8
ZnSe	0.29	3.2	−1.2	−1.3	0.31	3.3	−1.4	−1.5	0.25	2.6	−1.1	−1.2
ZnO	0.33	3.7	−2.2	−2.1	0.45	4.4	−2.4	−2.7	0.45	2.8	−1.5	−1.9
TiO_2	0.24	3.9	−1.2	−0.9	0.35	4.2	−1.2	−1.4	0.32	3.4	−0.6	−0.9
MgO	0.45	8.9	−3.0	−2.9	0.46	9.0	−3.0	−3.2	0.30	7.3	−2.0	−2.1

materials for different α in the PBE0 hybrid functional. Compared to PBE, the default mixing of 25% Fock exchange noticeably improves the description of the lattice parameters, showing an MAE of 0.02 Å with respect to the reference value derived from experiment (cf. Table VIII). The good agreement with experiment is preserved, and even enhanced with the empirical and nonempirical mixing parameters. Indeed, we find that the lattice parameters depend moderately on α, in accord with earlier studies [77,78]. In the most significant case where the mixing parameter increases from the default 0.25 to the nonempirical value of 0.45 for MgO, the change in the lattice constant a is merely 0.03 Å. Hence, the optimal mixing parameters can be regarded as globally effective, not only for the band gap but also for the structural parameters.

VII. BENCHMARKING OF BAND-EDGE POSITIONS: IONIZATION POTENTIALS

The accuracy of the band-edge positions obtained from various DFT and GW methods is assessed in this section through the calculation of ionization potentials (IPs). We consider eight semiconductor surfaces for which experimental IPs are available, including the (111) 2×1 reconstructed surface (i.e., the π-chain model [79]) for Si, Ge, and diamond; the (110) surface of zinc-blende GaAs, GaP, ZnSe, and rutile TiO_2; and the $(10\bar{1}0)$ surface of ZnO. We employ the slab model to calculate the IP of the solids. The IP is formally defined as the energy difference between the vacuum level $E_{\rm vac}$ and the VBM. To speed up the convergence with the thickness of the slab, it is convenient to determine the VBM in a separate bulk calculation and to align it to the electronic structure in the slab calculation through a local reference potential $V_{\rm ref}$. For $V_{\rm ref}$, we here consider the sum of the local potential and the electrostatic potential. The IP is then calculated as

$$\mathrm{IP} = \left(E_{\rm vac} - V_{\rm ref}^{\rm s}\right) - \left(\varepsilon_{\rm VBM}^{\rm b} - V_{\rm ref}^{\rm b}\right), \tag{13}$$

where the superscripts s and b refer to the slab and the bulk, respectively. Equation (13) is valid as long as the measurement is not drastically perturbed by the surface states. The slab model is taken sufficiently thick so that the local reference potential inside the slab corresponds to that of the bulk. More specifically, we use a slab of 13 atomic layers for the (110) surface of the zinc-blende structures. For the (111) reconstructed surface of Si, Ge, and diamond, a slab model of 24 atomic layers is used. The other surfaces are modeled by a slab of 12 atomic layers. The thickness of the vacuum region is chosen to be the same as that of the slab. During structural relaxation, several layers in the middle of the slab are fixed at their bulk positions. Detailed parameters in the slab calculations are given in Table IX.

To obtain IPs within the semilocal PBE, we calculate the quantities of both the bulk and the slab in Eq. (13) self-consistently. Slab calculations become cumbersome at higher theoretical levels and are eventually intractable in the GW approximation. Nevertheless, it has been found

TABLE VIII. The theoretical lattice parameters are compared to reference values obtained by subtracting out the zero-point anharmonic expansion [72,73] from the experimental values. Such contributions amount to $0.01 - 0.02$ Å. The experimental values are taken from Refs. [74–76]. The values of the empirical $\alpha^{\rm PBE0}$ and nonempirical $\overline{\alpha}_A$ are given in Tables VI and VII. For the wurtzite ZnO and rutile TiO_2, the c/a ratio is not varied and corresponds to the value obtained from the PBE optimization.

	PBE	PBE0(0.25)	PBE0($\alpha^{\rm PBE0}$)	PBE0($\overline{\alpha}_A$)	Ref.
Si	5.47	5.44	5.46	5.44	5.42
ZnSe	5.72	5.67	5.66	5.67	5.66
ZnO	3.28	3.24	3.23	3.23	3.22
TiO_2	4.64	4.59	4.64	4.59	4.58
MgO	4.26	4.21	4.19	4.18	4.19
ME (Å)	0.06	0.02	0.02	0.01	
MAE (Å)	0.06	0.02	0.02	0.01	
MARE (%)	1.4	0.4	0.5	0.3	

TABLE IX. Number of layers and **k**-point sampling used in the slab calculations. The number of layers that are kept fixed during the structural relaxation is given in parentheses.

	Number of layers	**k**-point mesh
Ge(111)	24 (4)	$6 \times 4 \times 1$
Si(111)	24 (4)	$6 \times 4 \times 1$
C(111)	24 (4)	$6 \times 4 \times 1$
GaAs(110)	13 (3)	$6 \times 4 \times 1$
GaP(110)	13 (3)	$6 \times 4 \times 1$
ZnSe(110)	13 (3)	$6 \times 4 \times 1$
ZnO$(10\bar{1}0)$	12 (4)	$6 \times 4 \times 1$
TiO_2(110)	12 (6)	$6 \times 4 \times 1$

TABLE X. Ionization potentials (in eV) of various semiconductor surfaces. The PBE values are obtained from self-consistent slab calculations. PBE0 and GW values are obtained by applying the corresponding bulk corrections to the PBE results. The notations of the methods follow the convention described in Table III.

	PBE	PBE0(α)	PBE0($\bar{\alpha}_A$)	$G_0W_0(0)$	$G_0W_0(\alpha)$	$G_0W_0(\bar{\alpha}_A)$	$G_0W_0^{\rm PBE}(\bar{\alpha}_C)$	QS$GW_0^{\rm PBE}$	Expt.
Ge(111)	4.37	4.75	4.78	4.99	5.08	5.20	5.11	5.24	4.80[a],4.74[b]
Si(111)	4.98	5.26	5.57	5.64	5.64	5.83	5.69	5.81	5.10[a], 5.25[c], 5.35[d]
C(111)	5.59	6.25	6.76	6.54	6.47	6.94	6.66	6.70	6.50[e]
GaAs(110)	4.71	5.21	5.33	5.32	5.46	5.56	5.38	5.48	5.47[a], 5.56[f]
GaP(110)	5.38	5.84	6.08	6.15	6.15	6.40	6.22	6.38	6.01[f]
ZnSe(110)	5.58	6.51	6.76	6.51	6.75	6.92	6.64	6.76	6.82[g]
ZnO(10$\bar{1}$0)	5.97	7.88	8.12	7.05	7.86	8.03	7.49	7.85	7.82[g]
TiO_2(110)	7.30	8.14	8.51	7.70	7.70	8.23	7.78	8.24	8.0[h], 8.2[i]
ME (eV)	−0.86	−0.11	0.14	−0.11	0.04	0.29	0.03	0.24	
MAE (eV)	0.86	0.15	0.21	0.31	0.18	0.29	0.26	0.24	
MARE (%)	13.0	2.4	3.1	4.7	3.0	5.1	4.3	4.2	

[a]Reference [81].
[b]Reference [82].
[c]Reference [83].
[d]Reference [84].
[e]Reference [85].
[f]Reference [86].
[g]Reference [87].
[h]Reference [88].
[i]Reference [89].

that a PBE description of the electrostatic potential is often adequate [4,6,33,80]. Here, we find that in the case of the Si(111) 2×1 reconstructed surface, the electrostatic potential $E_{\rm vac} - V^s_{\rm ref}$ differs by merely 0.02 eV between the PBE and the PBE0(0.25) calculations. For the more ionic TiO_2(110) surface, the difference is still within 0.1 eV. Further, the band-offset study of Shaltaf *et al.* revealed a limited variation (20 meV) of the electrostatic potential at the Si/SiO_2 interface at the QSGW level [33]. We hence infer that the use of the PBE electrostatic potential is a reasonable approximation for the calculations of the IP. Here, IPs within the PBE0 and GW schemes are thus determined by applying the bulk VBM shifts to the PBE lineup. We estimate that such a scheme introduces an error in the VBM positions of at most 0.1 eV in fully self-consistent PBE0 and GW calculations (one-shot G_0W_0 calculations are not affected since the charge density remains unmodified), and this should be taken into account when comparing the theoretical IPs to experimental values.

In addition to the standard PBE, the one-shot $G_0W_0(0)$, and the self-consistent QS$GW_0^{\rm PBE}$, we consider the empirically tuned PBE0(α) and $G_0W_0(\alpha)$, and the nonempirically tuned PBE0($\bar{\alpha}_A$), $G_0W_0(\bar{\alpha}_A)$, and $G_0W_0^{\rm PBE}(\bar{\alpha}_C)$, as introduced in Sec. VI. We do not take into account the QSGW and $G_0W_0(\bar{\alpha}_B)$ schemes as they overestimate band gaps and thereby tend to predict too large IPs.

The calculated IPs are reported in Table X. We also plot the calculated IPs against the experimental values in Fig. 7. Apart from the PBE which significantly underestimates the IPs with a mean absolute error (MAE) of nearly 0.9 eV, all the other methods predict the IPs reasonably well. In particular, the PBE0 hybrid functional yields excellent IPs over the whole set of surfaces, particularly when it is empirically tuned. This substantiates the use of hybrid functionals as a practical tool in electronic-structure calculations.

Let us now focus on the performance of the various GW schemes. The standard one-shot G_0W_0 on top of PBE already produces IPs that are in good agreement with experiment, and the errors are found to correlate with the quality of the predicted band gaps. In the case of semiconductors with shallow $3d$ bands (e.g., GaAs, ZnO, and ZnSe) for which $G_0W_0(0)$ underestimates the band gaps, the calculated IPs are too small as well. The band-gap issue is lifted in the empirical

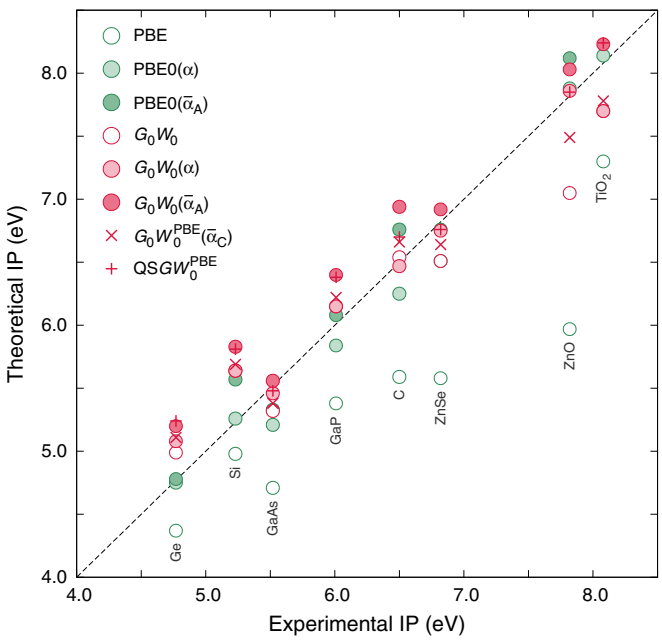

FIG. 7. (Color online) Ionization potentials (theoretical vs experimental) of various semiconductor surfaces. The data are taken from Table X. For systems with multiple experimental references, the adopted experimental IP corresponds to the average value.

G_0W_0 method, which brings the IPs of the $3d$ semiconductors closer to experimental values and scores a MAE smaller than 0.2 eV. However, the IP of rutile TiO_2 remains underestimated by as much as 0.4 eV within the one-shot $G_0W_0(0)$ method even though the band gap is well accounted for. This evidences the problematic band-edge positions of TiO_2 obtained with the PBE starting point.

The two nonempirically tuned G_0W_0 schemes considered in this section achieve a comparable MAE, but they behave somehow differently. With the optimal mixing parameter $\overline{\alpha}_A$, the calculated IPs are larger than the experimental values by a mean error (ME) of $\sim$0.3 eV as a result of the too large band gaps. The other nonempirical scheme $G_0W_0^{\mathrm{PBE}}(\overline{\alpha}_C)$ describes the IPs as well as the self-consistent $\mathrm{QS}GW_0^{\mathrm{PBE}}$ does, except for ZnO and TiO_2. In particular, we note that the problematic IP of TiO_2 found in the one-shot G_0W_0 calculations is successfully remedied with the self-consistent treatment in $\mathrm{QS}GW_0^{\mathrm{PBE}}$.

We note that the IPs within GW give an overestimation by about 0.3 eV for semiconductors such as Si, Ge, GaP, and diamond. Grüneis *et al.* recently reported that, for semiconductors, the additional inclusion of ladder diagrams (or vertex corrections) in the screened interaction and the self-energy shift the band-edge states (mostly the VBM) upward by 0.2−0.3 eV relative to the standard GW approximation [90]. This renormalization of the VBM compensates for the overestimation of the IPs seen in our GW calculations. As a further implication, the QP correction to the VBM is expected to be less predominant for semiconductors when vertex corrections are taken into account in GW.

VIII. CONCLUSIONS

We extensively studied the effect of starting point and self-consistency within the GW method on the band-edge positions of semiconductors and insulators. The dependence of starting point was investigated by one-shot G_0W_0 calculations on top of hybrid-functional calculations with varying fraction of Fock exchange α, whereas self-consistency was considered within the QP picture. Compared to G_0W_0 on top of PBE, the use of a PBE0 hybrid-functional starting point enhances the shifts of both the VBM and the CBM. At variance, the inclusion of self-consistency generally enhances the downwards shift of the VBM while leaving the CBM less perturbed. Overall, when compared to G_0W_0 on top of PBE, the predominant role of the VBM shift in the band-gap opening is maintained. However, for transition-metal compounds, the semilocal starting point is less adequate particularly for the CBM. As a result, the band-edge positions of TiO_2 and MoS_2 show a qualitative difference between the one-shot calculation on top of PBE and the self-consistent calculation.

We next sought optimal mixing parameters α to be used in the starting point for G_0W_0 calculations in the context of empirical and nonempirical tuning. When tuned empirically to reproduce the experimental band gap, PBE0 and G_0W_0 show distinct band-edge positions, which differ up to 0.3 eV for sp semiconductors. The difference reduces in the nonempirical scheme in which α is varied until the PBE0 starting point and the subsequent G_0W_0 calculations achieve the same band gap, although the band gaps are then normally overestimated. We further proposed two other nonempirical tuning schemes in which the band gap achieved in $G_0W_0(\alpha)$ is matched to that in either $\mathrm{QS}GW$ or $\mathrm{QS}GW_0^{\mathrm{PBE}}$. In both cases, we recorded a good agreement of the band-edge positions (typically within 0.2 eV) between one-shot G_0W_0 on top of the optimal starting point and the corresponding self-consistent calculations.

The accuracy of the band-edge positions was finally estimated by addressing ionization potentials at surfaces. We found that the description of ionization potentials improves with that of the band gap, as both empirically tuned PBE0 and G_0W_0 yield good ionization potentials. Moreover, the one-shot G_0W_0 which reproduces the band gap achieved with $\mathrm{QS}GW_0^{\mathrm{PBE}}$ showed comparable accuracy with its more computationally demanding self-consistent counterpart. Nevertheless, for systems such as TiO_2 and MoS_2, the prescription of self-consistency is necessary in order to obtain a reasonable ionization potential. For these materials, a starting point beyond the semilocal description or ideally a self-consistent treatment is therefore warranted whenever the absolute positions of the band edges are important.

ACKNOWLEDGMENTS

We thank F. Bruneval, G. Kresse, and G.-M. Rignanese for interesting discussions. This work is supported by the Swiss National Science Foundation (Grants No. 200020-134600 and No. 200020-152799). We used computational resources of CSEA-EPFL and CSCS.

[1] C. G. Van de Walle and R. M. Martin, Phys. Rev. B **35**, 8154 (1987).
[2] A. Alkauskas, P. Broqvist, and A. Pasquarello, Phys. Rev. Lett. **101**, 046405 (2008); Phys. Status Solidi B **248**, 775 (2011).
[3] A. Alkauskas and A. Pasquarello, Phys. Rev. B **84**, 125206 (2011).
[4] K. Steiner, W. Chen, and A. Pasquarello, Phys. Rev. B **89**, 205309 (2014).
[5] A. J. Nozik, Annu. Rev. Phys. Chem. **29**, 189 (1978).
[6] A. Alkauskas, P. Broqvist, F. Devynck, and A. Pasquarello, Phys. Rev. Lett. **101**, 106802 (2008).
[7] H.-P. Komsa, P. Broqvist, and A. Pasquarello, Phys. Rev. B **81**, 205118 (2010).
[8] H.-P. Komsa and A. Pasquarello, Phys. Rev. B **84**, 075207 (2011).
[9] R. Ramprasad, H. Zhu, P. Rinke, and M. Scheffler, Phys. Rev. Lett. **108**, 066404 (2012).
[10] W. Chen and A. Pasquarello, Phys. Rev. B **88**, 115104 (2013).
[11] J. P. Perdew, K. Burke, and M. Ernzerhof, Phys. Rev. Lett. **77**, 3865 (1996).
[12] H. Jiang and Y.-C. Shen, J. Chem. Phys. **139**, 164114 (2013).
[13] S. Kümmel and L. Kronik, Rev. Mod. Phys. **80**, 3 (2008).
[14] L. Hedin, Phys. Rev. **139**, A796 (1965).
[15] W. Chen and A. Pasquarello, Phys. Rev. B **86**, 035134 (2012); **88**, 119906(E) (2013).
[16] M. S. Hybertsen and S. G. Louie, Phys. Rev. B **34**, 5390 (1986).

[17] M. Shishkin and G. Kresse, Phys. Rev. B **75**, 235102 (2007).
[18] F. Fuchs, J. Furthmüller, F. Bechstedt, M. Shishkin, and G. Kresse, Phys. Rev. B **76**, 115109 (2007).
[19] S. V. Faleev, M. van Schilfgaarde, and T. Kotani, Phys. Rev. Lett. **93**, 126406 (2004).
[20] M. van Schilfgaarde, T. Kotani, and S. Faleev, Phys. Rev. Lett. **96**, 226402 (2006).
[21] F. Bruneval, N. Vast, and L. Reining, Phys. Rev. B **74**, 045102 (2006).
[22] J. P. Perdew, M. Ernzerhof, and K. Burke, J. Chem. Phys. **105**, 9982 (1996).
[23] T. Kotani, M. van Schilfgaarde, and S. V. Faleev, Phys. Rev. B **76**, 165106 (2007).
[24] B. Holm and U. von Barth, Phys. Rev. B **57**, 2108 (1998).
[25] X. Gonze, B. Amadon, P.-M. Anglade, J.-M. Beuken, F. Bottin, P. Boulanger, F. Bruneval, D. Caliste, R. Caracas, M. Côté, T. Deutsch, L. Genovese, P. Ghosez, M. Giantomassi, S. Goedecker, D. Hamann, P. Hermet, F. Jollet, G. Jomard, S. Leroux, M. Mancini, S. Mazevet, M. Oliveira, G. Onida, Y. Pouillon, T. Rangel, G.-M. Rignanese, D. Sangalli, R. Shaltaf, M. Torrent, M. Verstraete, G. Zerah, and J. Zwanziger, Comput. Phys. Commun. **180**, 2582 (2009).
[26] W. Luo, S. Ismail-Beigi, M. L. Cohen, and S. G. Louie, Phys. Rev. B **66**, 195215 (2002).
[27] M. L. Tiago, S. Ismail-Beigi, and S. G. Louie, Phys. Rev. B **69**, 125212 (2004).
[28] A. Alkauskas and A. Pasquarello, Physica B: Condens. Matter (Amsterdam) **401-402**, 670 (2007).
[29] F. Tran, Phys. Lett. A **376**, 879 (2012).
[30] F. Gygi and A. Baldereschi, Phys. Rev. B **34**, 4405 (1986).
[31] S. Lebègue, B. Arnaud, M. Alouani, and P. E. Bloechl, Phys. Rev. B **67**, 155208 (2003).
[32] R. W. Godby and R. J. Needs, Phys. Rev. Lett. **62**, 1169 (1989).
[33] R. Shaltaf, G.-M. Rignanese, X. Gonze, F. Giustino, and A. Pasquarello, Phys. Rev. Lett. **100**, 186401 (2008).
[34] M. Stankovski, G. Antonius, D. Waroquiers, A. Miglio, H. Dixit, K. Sankaran, M. Giantomassi, X. Gonze, M. Côté, and G.-M. Rignanese, Phys. Rev. B **84**, 241201 (2011).
[35] P. Larson, M. Dvorak, and Z. Wu, Phys. Rev. B **88**, 125205 (2013).
[36] B.-C. Shih, Y. Xue, P. Zhang, M. L. Cohen, and S. G. Louie, Phys. Rev. Lett. **105**, 146401 (2010).
[37] P. Broqvist, A. Alkauskas, and A. Pasquarello, Phys. Rev. B **80**, 085114 (2009); **81**, 039903(E) (2010).
[38] P. Carrier, S. Rohra, and A. Görling, Phys. Rev. B **75**, 205126 (2007).
[39] F. Gygi, Ph.D. thesis, École Polytechnique Fédérale Lausanne, 1988.
[40] S. Massidda, M. Posternak, and A. Baldereschi, Phys. Rev. B **48**, 5058 (1993).
[41] O. Madelung, *Semiconductor-Basic Data*, 2nd ed. (Springer, New York, 1996).
[42] J. Lüning, S. Eisebitt, J.-E. Rubensson, C. Ellmers, and W. Eberhardt, Phys. Rev. B **59**, 10573 (1999).
[43] I. Vurgaftman and J. R. Meyer, J. Appl. Phys. **94**, 3675 (2003).
[44] M. R. Lorenz, G. D. Pettit, and R. C. Taylor, Phys. Rev. **171**, 876 (1968).
[45] A. Mang, K. Reimann, and S. Rbenacke, Solid State Commun. **94**, 251 (1995).
[46] R. H. Bube, Phys. Rev. **98**, 431 (1955).
[47] K. F. Mak, C. Lee, J. Hone, J. Shan, and T. F. Heinz, Phys. Rev. Lett. **105**, 136805 (2010).
[48] Y. Tezuka, S. Shin, T. Ishii, T. Ejima, S. Suzuki, and S. Sato, J. Phys. Soc. Jpn. **63**, 347 (1994).
[49] S.-G. Lim, S. Kriventsov, T. N. Jackson, J. H. Haeni, D. G. Schlom, A. M. Balbashov, R. Uecker, P. Reiche, J. L. Freeouf, and G. Lucovsky, J. Appl. Phys. **91**, 4500 (2002).
[50] T. DiStefano and D. Eastman, Solid State Commun. **9**, 2259 (1971).
[51] D. M. Roessler and W. C. Walker, Phys. Rev. **159**, 733 (1967).
[52] M. Piacentini, D. W. Lynch, and C. G. Olson, Phys. Rev. B **13**, 5530 (1976).
[53] J. P. Perdew, R. G. Parr, M. Levy, and J. L. Balduz, Phys. Rev. Lett. **49**, 1691 (1982).
[54] J. P. Perdew and M. Levy, Phys. Rev. Lett. **51**, 1884 (1983).
[55] L. J. Sham and M. Schlüter, Phys. Rev. Lett. **51**, 1888 (1983).
[56] R. W. Godby, M. Schlüter, and L. J. Sham, Phys. Rev. Lett. **56**, 2415 (1986).
[57] M. Grüning, A. Marini, and A. Rubio, J. Chem. Phys. **124**, 154108 (2006).
[58] P. Mori-Sánchez, A. J. Cohen, and W. Yang, Phys. Rev. Lett. **100**, 146401 (2008).
[59] M. A. L. Marques, J. Vidal, M. J. T. Oliveira, L. Reining, and S. Botti, Phys. Rev. B **83**, 035119 (2011).
[60] C. Friedrich, M. C. Müller, and S. Blügel, Phys. Rev. B **83**, 081101 (2011).
[61] A. N. Chantis, M. van Schilfgaarde, and T. Kotani, Phys. Rev. Lett. **96**, 086405 (2006).
[62] A. Svane, N. E. Christensen, M. Cardona, A. N. Chantis, M. van Schilfgaarde, and T. Kotani, Phys. Rev. B **81**, 245120 (2010).
[63] M. Shishkin, M. Marsman, and G. Kresse, Phys. Rev. Lett. **99**, 246403 (2007).
[64] S. Botti and M. A. L. Marques, Phys. Rev. Lett. **110**, 226404 (2013).
[65] F. Giustino, S. G. Louie, and M. L. Cohen, Phys. Rev. Lett. **105**, 265501 (2010).
[66] E. Cannuccia and A. Marini, Phys. Rev. Lett. **107**, 255501 (2011).
[67] C. E. Patrick and F. Giustino, J. Phys.: Condens. Matter **24**, 202201 (2012).
[68] N. Marom, J. E. Moussa, X. Ren, A. Tkatchenko, and J. R. Chelikowsky, Phys. Rev. B **84**, 245115 (2011).
[69] T. Körzdörfer and N. Marom, Phys. Rev. B **86**, 041110 (2012).
[70] V. Atalla, M. Yoon, F. Caruso, P. Rinke, and M. Scheffler, Phys. Rev. B **88**, 165122 (2013).
[71] N. A. Richter, S. Sicolo, S. V. Levchenko, J. Sauer, and M. Scheffler, Phys. Rev. Lett. **111**, 045502 (2013).
[72] A. B. Alchagirov, J. P. Perdew, J. C. Boettger, R. C. Albers, and C. Fiolhais, Phys. Rev. B **63**, 224115 (2001).
[73] P. Hao, Y. Fang, J. Sun, G. I. Csonka, P. H. T. Philipsen, and J. P. Perdew, Phys. Rev. B **85**, 014111 (2012).
[74] H. Karzel, W. Potzel, M. Köfferlein, W. Schiessl, M. Steiner, U. Hiller, G. M. Kalvius, D. W. Mitchell, T. P. Das, P. Blaha, K. Schwarz, and M. P. Pasternak, Phys. Rev. B **53**, 11425 (1996).
[75] C. J. Howard, T. M. Sabine, and F. Dickson, Acta Crystallogr. B **47**, 462 (1991).
[76] L. Schimka, J. Harl, and G. Kresse, J. Chem. Phys. **134**, 024116 (2011).

[77] P. Deák, A. Gali, A. Sólyom, A. Buruzs, and T. Frauenheim, J. Phys.: Condens. Matter **17**, S2141 (2005).
[78] D. Koller, P. Blaha, and F. Tran, J. Phys.: Condens. Matter **25**, 435503 (2013).
[79] K. C. Pandey, Phys. Rev. Lett. **47**, 1913 (1981).
[80] J. L. Lyons, A. Janotti, and C. G. Van de Walle, Phys. Rev. B **80**, 205113 (2009).
[81] G. W. Gobeli and F. G. Allen, Phys. Rev. **137**, A245 (1965).
[82] G. Guichar, G. Garry, and C. Sébenne, Surf. Sci. **85**, 326 (1979).
[83] F. J. Himpsel, G. Hollinger, and R. A. Pollak, Phys. Rev. B **28**, 7014 (1983).
[84] C. Sebenne, D. Bolmont, G. Guichar, and M. Balkanski, Phys. Rev. B **12**, 3280 (1975).
[85] F. J. Himpsel, D. E. Eastman, and J. F. van der Veen, J. Vac. Sci. Technol. **17**, 1085 (1980).
[86] J. van Laar, A. Huijser, and T. L. van Rooy, J. Vac. Sci. Technol. **14**, 894 (1977).
[87] R. K. Swank, Phys. Rev. **153**, 844 (1967).
[88] G. Xiong, R. Shao, T. Droubay, A. Joly, K. Beck, S. Chambers, and W. Hess, Adv. Funct. Mater. **17**, 2133 (2007).
[89] K. Schierbaum, S. Fischer, M. Torquemada, J. de Segovia, E. Román, and J. Martín-Gago, Surf. Sci. **345**, 261 (1996).
[90] A. Grüneis, G. Kresse, Y. Hinuma, and F. Oba, Phys. Rev. Lett. **112**, 096401 (2014).